Materials Science & Engineering A 974 (2026) 150881

Contents lists available at ScienceDirect

Materials Science & Engineering A

journal homepage: www.elsevier.com/locate/msea

Influence of Mo and Cu additions on the microstructure and mechanical performance of air-hardening ductile forging steels in the context of circular economy

Oguz Gulbay [a,*], Oyku Guner [a], Adam Skowronek [b], Aleksandra Kozłowska [c], Adam Grajcar [c], Ulrich Krupp [a], Alexander Gramlich [a]

[a] Steel Institute, RWTH Aachen University, Aachen, 52072, Germany
[b] Materials Research Laboratory, Faculty of Mechanical Engineering, Silesian University of Technology, Gliwice, Poland
[c] Department of Engineering Materials and Biomaterials, Faculty of Mechanical Engineering, Silesian University of Technology, Gliwice, Poland

ARTICLE INFO

Keywords:
Martensite
Bainite
Air-hardening
Ductile
Forging
Copper

ABSTRACT

The increasing reliance and usage of recycled steel in the global steel industry brings the need for a scientific assessment of alloying concepts that remain robust against recycling-induced variations in steel composition. In this study, the influence of elevated Mo and Cu concentrations, representing exaggerated recycling-induced alloying elements, on the microstructure and mechanical performance of cost-effective air-hardening ductile (AHD) forging steels is systematically investigated. The results show that both elements improve the hardenability of the steels by delaying diffusional and bainitic transformations, increasing the maximum possible thickness of forging components that can be produced via air cooling. Cu alloying significantly controls the prior austenite grain size, most likely through a solute drag effect in solid solution. Among the achieved microstructures, the fully martensitic state exhibits the most favorable mechanical property profile, combining the highest strength under static and cyclic loading, adequate ductility, and the highest impact toughness. However, multiphase microstructures, containing bainite and martensite, display inconsistent trends in tensile ductility and impact toughness. Overall, the results suggest that recycling-induced Mo and Cu alloying can improve the mechanical performance of the AHD forging steels as long as Cu-induced hot shortness can be avoided during processing.

1. Introduction

Steel forgings are used for a variety of applications spanning small components within the automotive drive train up to rotor shafts in wind energy turbines. While up-to-date classic quench and tempering (QT) steels like C45 or 42CrMo4 dominate the market, new steel grades are continuously being developed with the aim of either increasing the performance or reducing the production costs of current steel grades. While air-hardening precipitation hardening ferritic-pearlitic (PHFP) as well as bainitic steels were developed several years ago [1], their application is limited due to their relatively low mechanical properties and reduced impact toughness or their complex and difficult-to-implement heat treatments, respectively.

Recently, air-hardened ductile (AHD) steels [2–6] have emerged as a promising alternative and have already found application in forging products such as connecting rods [7] and spring U-bolts [8]. They combine a cost-effective production route with mechanical properties matching those of QT steels. Moreover, their cyclic strength and fatigue properties have been shown to be superior [5], enabling lightweighting. Containing ~4 wt% manganese, AHD steels belong to the class of third-generation advanced high-strength steels (AHSS), specifically medium-manganese steels (MMnS) [9]. The comparatively high alloying levels in these steels delay diffusional transformations during air cooling, thereby promoting the formation of stronger displacive transformation products such as martensite and bainite [2]. However, achieving sufficient Charpy V-notch impact energy remains a significant challenge, mainly due to Mn-embrittlement, a phenomenon occurring when Mn segregates to grain boundaries and weakens them [10–12]. To address this issue and strengthen the grain boundaries, three main approaches have been identified: refining the prior austenite grain (PAG)

* Corresponding author.
E-mail address: oguz.guelbay@iehk.rwth-aachen.de (O. Gulbay).

https://doi.org/10.1016/j.msea.2026.150881
Received 2 March 2026; Received in revised form 6 July 2026; Accepted 2 August 2026
Available online 3 August 2026
0921-5093/© 2026 The Authors. Published by Elsevier B.V. This is an open access article under the CC BY license (http://creativecommons.org/licenses/by/4.0/).

size, alloying with molybdenum and boron to increase prior austenite grain boundary cohesion, as well as increasing the martensite start (M_s) temperature by the addition of aluminum, and hence increasing the self-tempering (auto-tempering) during air-cooling [13].

Originally, the alloying concept was designed for long products produced in the electric arc furnace. Hence, from the beginning, a relatively low quantity of residual elements (e.g., Ni, Cu, Cr) originating from steel recycling was added to the laboratory melts to imitate real industrial melts with high recycling rates. As alloyed steels tend to show, in general, lower susceptibility to tramp elements like Cu [14], the question arises if the AHD steels might be able to act as a sink for low-quality scraps and if the beneficial effect of the tramp elements (like increasing the hardenability [15,16]) can be used. In general, the effect of Cu and Mo on the mechanical properties of alloyed martensitic steels, can be regarded as positive for most applications. Both elements retard diffusion based phase transformation and therefore increase the hardenability, which allows the production of components which larger wall thickness. The strength and hardness can be increased by additions of Cu and Mo, either by the precipitation of Cu precipitates or molybdenum carbides, or by interacting with the cementite precipitation kinetics [17]. To date, the individual effects of Mo and Cu additions have been investigated sporadically in multiphase steels with retained austenite containing above 6 wt% Mn [18–21] or below 1 wt% Mn [22], typically produced via multi-stage heat treatment or thermomechanical processing. However, systematic and comparative studies addressing the combined effect of these elements in cost- and energy-efficient AHD steels containing 4 wt% Mn are lacking.

Aligned with the steel industry's transition to a circular economy, this study investigates how elevated concentrations of Mo and Cu influence the microstructure and mechanical properties of AHD steels for forging components, while exploring their potential to enhance recyclability and overcome current performance limitations, particularly with respect to impact toughness. To this end, three AHD steel variants with systematically varied Mo and Mo-Cu contents were produced under industrially relevant air-hardening conditions after forging. Firstly, the microstructure of each variant is investigated using light optical microscopy (LOM), scanning-electron microscopy (SEM) and electron backscattered diffraction (EBSD) on the same region of interests (ROI), enabling a direct cross-method correlation that allows microstructural features observed with different methods to be linked to one another. Particular attention is given to the role of Cu in refining the PAG size, which additionally can be classified as a potential benefit of elevated tramp element concentrations. The microstructural characterization is further supported by X-Ray diffraction (XRD) analysis to complement and validate the findings. Subsequently, the corresponding mechanical properties are determined using tensile, hardness, instrumented Charpy impact and cyclic load increase tests (LIT) to reflect the industrial relevance for forging applications, supported by fracture surface analyses. This combination of testing methods further enables the achieved microstructures to be linked with the mechanical response under various loading scenarios, providing a comprehensive and comparative understanding of the structure-property relationships across the studied AHD forging steels.

Beyond this, the study clarifies the distinct roles of Mo and Cu in the transformation behavior and properties of 4 wt% Mn AHD steels. The influence of Mo and Cu is discussed mechanistically, showing how both elements retard the bainitic transformation and improve hardenability, promoting an increasing martensite fraction via air cooling, while Cu additionally limits PAG growth through a solute drag effect. Linking these transformation mechanisms to the air-cooled microstructures and their static, dynamic, and cyclic properties demonstrates how recycling-induced tramp elements can be deliberately used rather than only tolerated in the design of recycling-compatible forging steels.

2. Materials and methods

Three steel ingots (80 kg) were cast in a laboratory-scale vacuum induction furnace. The ingots with a cross-section of $140 \times 140\,mm^2$ were homogenized for 5 h at 1200 °C and consecutively forged into billets with a final cross-section of 60 x 60 mm^2. The forging temperature was kept between 1200 °C and 1100 °C, controlled with a pyrometer. After forging, the billets were air-cooled to room temperature. Each steel was primarily alloyed with 4 wt% manganese to retard the diffusion-controlled and bainite transformations, thereby enhancing hardenability. Silicon and aluminum were alloyed to suppress carbide precipitation and coarsening, while Nb was alloyed for austenite grain size control during forging. To investigate the influence of molybdenum and copper, one steel was additionally alloyed with 0.3 wt.-% Mo, and another one with 0.3 wt.-% molybdenum and 1.0 wt.-% copper. The concentrations were derived from different scenarios and assumptions: the current largest sinks for Cu contaminated scrap fractions are rebars, with concentrations up to 0.8 wt%; to provide a more resilient sink for Cu, concentrations beyond this value must be considered. Mo, as a tramp element, reaches concentrations between 0.1 and 0.2 wt% depending on the scrap fractions used. Lower values require the utilization of clean production scraps (e.g., from automotive sheet production). To address future scenarios, an increased concentration of 0.3 wt % was considered. Based on their chemical compositions, the three investigated steels are referred to as Ref, 0.3Mo-0Cu, and 0.3Mo-1Cu. The measured chemical compositions, determined via spark emission spectroscopy, are shown in Table 1.

The uniaxial tensile tests were conducted using B6 x 30 cylindrical specimens with a gauge diameter of 6 and a gauge length of 30 mm. The tests were performed at room temperature on a ZWICKROELL Z100 universal electromechanical testing machine (ZwickRoell GmbH & Co. KG, Germany) at a strain rate of $0.0025\,s^{-1}$. Three tensile specimens were tested for each steel. Charpy impact tests were conducted on a 300 J Instrumented Charpy impact test equipment using standard V-notched 10 x $10 \times 55\,mm^3$ specimens. The specimens were extracted parallel to the forging direction, with a notch machined perpendicular to the forging direction. For each steel, three tests were performed. The hardness of the materials was determined using Vickers 10 (HV10) indentation with a holding time of 15 s. In order to estimate the technical fatigue limit and gain insight into the resistance of the studied steels against cyclic loading under high-cycle fatigue (HCF) regimes, load increase tests (LIT) were performed. The LITs were performed on M16 cylindrical specimens with a minimum diameter of 4 mm and a total length of 85.The tests performed on a RUMUL GIGAFORTE 50 (Russenberger Prüfmachinen AG, Switzerland) resonant testing machine with a testing frequency of 1 kHz and a stress ratio of $R = -1$. All specimens were mechanically polished with diamond paste down to 1 μm to ensure a high-quality surface finish. Tests were initiated at a predefined stress amplitude and maintained for 10^6 cycles. After each 10^6-cycle interval, the stress amplitude was increased by 10 MPa. This procedure was repeated until failure, while the surface temperature was continuously monitored using a thermocouple, and no external cooling was applied. While the fatigue limit is conventionally approximated by identifying the transition point at which the monitored temperature response deviates from its baseline level particularly in low testing conditions [23,24], the high frequency testing conditions at 1 kHz cause a more pronounced thermal signal compared to low frequency. Therefore, in this study, the stress amplitude corresponding to a sudden and significant jump was taken as the estimate of the technical fatigue limit of the respective steel as the energy dissipation per cycle and the associated thermal signal cannot be straightforwardly interpretable. This interpretation approach follows the methodology established in a prior study on bainitic steels, where promising agreement was demonstrated between fatigue limits determined via the staircase method and LIT-based estimates across four different bainite groups [25]. Beyond fatigue limit estimation, LIT is particularly suitable for production

Table 1
Chemical composition of the investigated steels in wt.-%.

Steel	C	Mn	Si	Al	Nb	Mo	Cu	P	S
Ref	0.18	4.00	0.52	0.76	0.05	<0.005	0.01	0.003	0.003
0.3Mo-0Cu	0.17	4.02	0.51	0.75	0.05	0.30	0.01	0.004	0.004
0.3Mo-1Cu	0.17	4.10	0.52	0.79	0.05	0.30	1.04	0.003	0.008

accompanied testing, as it enables rapid verification of fatigue-relevant properties during manufacturing, allowing production parameters to be adjusted to achieve targeted mechanical performance [23]. For the same reason, it also serves as an effective comparative tool for systematically evaluating and ranking the fatigue performance of compositionally and microstructurally related alloy variants, in particular. Accordingly, the primary purpose of the LIT approach in the present study is to provide a comparative assessment of the fatigue performance of the investigated steels rather than to determine absolute fatigue limit values.

For the microstructural investigations of the undeformed material states, samples were extracted from the screw heads of the tensile specimens, with the examined surfaces oriented perpendicular to the forging direction. For the light optical microscopy (LOM) and scanning electron microscopy (SEM) investigations, the surface of the specimens was prepared by mechanical grinding up to 1200 grid SiC paper, followed by mechanical polishing with diamond paste of 6 µm and 1 µm, respectively. Subsequently, the polished surface of the specimens was etched with 3% HNO_3 (Nital) solution. LOM investigations were carried out using a Keyence light microscope, while SEM investigations were carried out on a field-emission gun ZEISS SIGMA SEM (Carl Zeiss Microscopy GmbH, Germany) using a secondary electron (SE) detector. The electron backscatter diffraction (EBSD) measurements were performed on a plasma-focused ion beam SEM Helios G5 PFIB/SEM (Thermo Fisher Scientific, Inc., Waltham, MA, USA) using an EDAX Velocity Super EBSD camera system with an accelerating voltage of 20 kV and an electron-beam current of 6.4 nA. For the post-processing of the EBSD data, the EDAX OIM Analysis software is used. To improve microstructural characterization and facilitate a direct correlation between the LOM, SEM, and EBSD results, all investigations were performed on the same region of interest (ROI) for each steel. For this purpose, a ROI was determined with Vickers hardness indentations as reference markers. After LOM and SEM investigations were completed, specimens were polished again with 1 µm diamond paste and underwent a final polishing step using oxide polishing suspension (OPS) for 10 min. The ROI to conduct EBSD measurements on the OPS polished specimens was located again by using the Vickers hardness indentations. Due to experimental constraints, the working distance could not be coupled to the stage coordinates during the measurements. Therefore, the absolute scaling of the ROI-EBSD maps was not correctly captured. Nevertheless, relative scale comparison remained possible by correlating the EBSD maps with the corresponding ROI-SEM images. Additionally, another set of EBSD measurements was conducted to investigate the PAG size of the investigated steels. The measurements were performed using ZEISS SIGMA SEM (Carl Zeiss Microscopy GmbH, Germany) equipped with a NordlysNano (Oxford Instruments, Great Britain) detector with a 75 µm aperture, an accelerating voltage of 20 kV, and a working distance of 17 mm. The post processing of the EBSD data to reconstruct the PAG of the investigated steels was done via Aztec Crystal EBSD processing software (Oxford Instruments) using Nishiyama-Wasserman orientation relationship. Additionally, linear intercept method is employed to quantitively determine the PAG size of the investigated steels. To ensure reliability, approximately 40-50 grains were included per condition, and the results are reported statistically. To reveal the PAG boundaries, the polished specimen surfaces were subjected to multiple sequential cycles of etching in picral solution followed by light surface polishing, until the boundaries became visible under LOM. To determine the retained austenite (RA) fraction of the investigated steels, X-ray diffraction (XRD) was performed using SEIFERT XRD 3003 PTS with a Cr Kα target, $2\theta = 60$ - $170°$. The sampling of the deformed tensile specimens was done approximately 10 mm from the fracture surface due to size restrictions in XRD measurements. The quantitative analysis of the XRD data was performed via the Rietveld method using Materials Analysis Using Diffraction (MAUD) software [26].

Dilatometry was employed to support microstructural findings obtained from air-cooled AHD steels. For the experiments, a Bähr high resolution DIL805A/D dilatometer and cylindrical specimens with dimensions of $\varnothing 5 \times 10$ mm were used. The experiments were conducted under vacuum atmosphere. The specimens were austenitized at 1000 °C for 300 s, followed by cooling to 900 °C, with a cooling rate of 5 K/s, and subsequent deformation to a 50% reduction at a strain rate of 1 s^{-1}. After deformation, the specimens were continuously cooled to room temperature at a cooling rate of 0.1 K/s, selected to replicate the average cooling rate of industrial air cooling. The deformation temperature of 900 °C was chosen to correspond to the industrial forging-end temperature.

3. Results

3.1. Microstructure evolution

Figs. 1 and 2 show the microstructural evolution of the investigated AHD steels as a function of Mo and Mo-Cu alloying. Fig. 1 presents correlated LOM, SEM, and EBSD analyses of selected region of interest (ROI), enabling direct correlation among the images obtained from different techniques, which allows us to identify and correlate microstructural features and constituent phases more accurately. Fig. 2 provides high-resolution higher-magnification SEM images for each steel state, offering an additional overview and supporting the interpretation of ROI-based observations, as the ROI-investigations were conducted at relatively low magnification, particularly to be able to locate the same region for EBSD analysis on the OPS-polished surface.

LOM images of the studied steels, assessing the macroscopic influence of Mo and Mo-Cu alloying on the air-cooled microstructure, are shown in Fig. 1a–c. The Ref steel exhibits a predominantly bainitic microstructure, revealed by blue coloration under LOM after Nital etching, along with martensitic regions as highlighted in Fig. 1a. With Mo alloying in 0.3Mo-0Cu, the martensite fraction visibly increases, while a significant amount of bainitic regions remain (cf. Fig. 1b). Further alloying with Cu in the 0.3Mo-1Cu results in a fully martensitic microstructure (cf. Fig. 1c).

The ROI-LOM of the Ref steel in Fig. 1d reveals the complexity of the microstructure, consisting of bainitic and martensitic regions, as highlighted in dashed regions. The corresponding SEM image of the same ROI uncovers further details regarding the morphology and distribution of RA in bainitic regions, exhibiting both film-like and blocky morphologies. As highlighted in a bainitic region by the red dashed area in Fig. 1g, film-like RA morphology is clearly visible between bainitic ferrite (BF) plates. This is further confirmed by the EBSD phase map in Fig. 1j on the same ROI, where the FCC phase is shown in red color. In addition, blocky RA is present in bulky form that is embedded in bainitic matrix, as shown in Fig. 1g–j. Furthermore, martensite-austenite (MA) islands also coexist, preferentially located in the vicinity of prior austenite grain boundaries (PAGB), as highlighted by the orange arrows in Fig. 1g, adding further complexity to the microstructure. These findings are also clearly visible in the high-resolution SEM image of the Ref steel in Fig. 2a. In martensitic region of the Ref steel, highlighted by

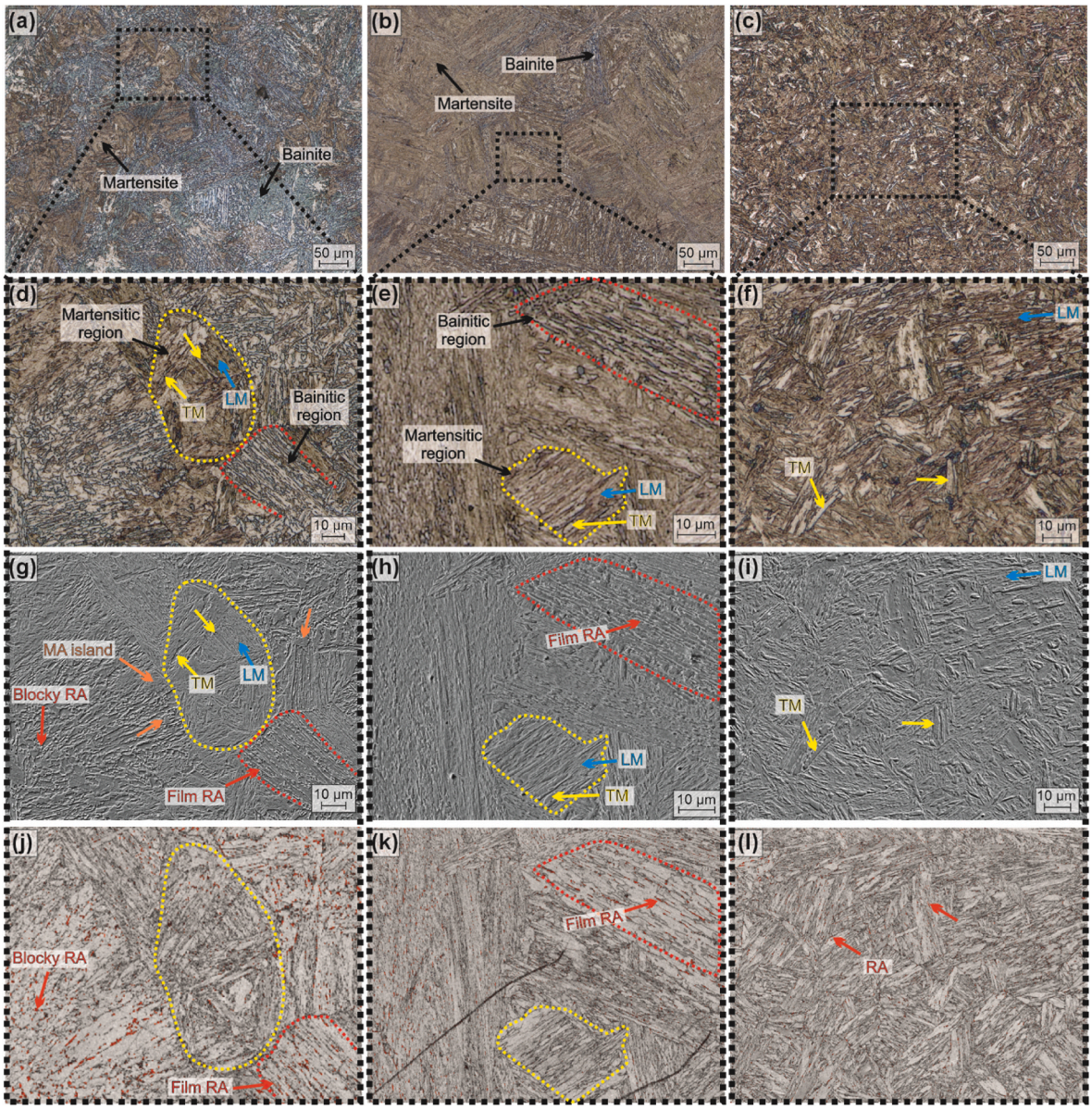


Fig. 1. LOM images of (a) Ref, (b) 0.3Mo-0Cu, and (c) 0.3Mo-1Cu, showing the microstructural overview, revealed by Nital etching. The dashed rectangles in (a–c) indicate the regions of interest (ROI) selected for detailed microstructural characterization. (d–f) Higher-magnification LOM images, (g–i) corresponding SEM micrographs, and (j–l) EBSD Fit maps superimposed with the FCC phase acquired from the ROIs marked in (a–c) for the Ref (d, g, j), 0.3Mo–0Cu (e, h, k), and 0.3Mo–1Cu (f, i, l) steels. (RA: Retained Austenite, MA: Martensite-Austenite, LM: Lath Martensite, TM: Tempered Martensite).

a yellow dashed area in Fig. 1d–g, a clear distinction can be observed between fresh martensite, characterized by fine lath structures (indicated by blue arrows), and auto-tempered martensite (indicated by yellow arrows), where laths appear locally coarsened with fine carbide precipitations.

In the case of 0.3Mo-0Cu, a similar overall microstructure is observed, as shown in Fig. 1e–h. However, the achieved microstructure is noticeably finer, particularly within the bainitic regions, characterized by finer RA films between BF plates compared to the Ref steel, as highlighted in Fig. 1h, which is confirmed by EBSD phase mapping shown in Fig. 1k. As a side note, based on SEM and EBSD results of 0.3Mo-0Cu steel, blocky RA and MA island formation is less frequently observed compared to the Ref steel. In Fig. 2b, it is also shown that the RA films are refined, while no block RA or MA island is observed in the vicinity of PAGBs.

In Fig. 1f–i, the LOM and SEM images of the corresponding ROI for the 0.3Mo-1Cu are shown, respectively. The higher-magnification images confirm a fully martensitic microstructure, consisting of fresh martensite and auto-tempered martensite (cf. Fig. 2c). It is observed that the tempered martensitic regions shown in the SEM image (cf. Fig. 1i) appear brighter in the LOM image of the corresponding ROI compared to the fresh martensitic areas (cf. Fig. 1f). Interestingly, in the lower-magnification LOM image (cf. Fig. 1c), these tempered martensitic regions exhibit a distinct bluish coloration, which is similar to the appearance of the bainitic regions observed in the other investigated steels (cf.Fig. 1a–b). In the corresponding EBSD phase map shown in Fig. 1l, small fractions of RA are indexed, and appear to be predominantly located along crystallographic boundaries such as lath, block and packet boundaries.

Since EBSD measurements may be insufficient for an accurate quantification of RA, quantitative XRD was employed to determine the RA fractions to support microstructural assessment. In particular, the spatial resolution of EBSD might be insufficient to detect thin RA films. Moreover, since it is a surface-sensitive technique, the measured RA

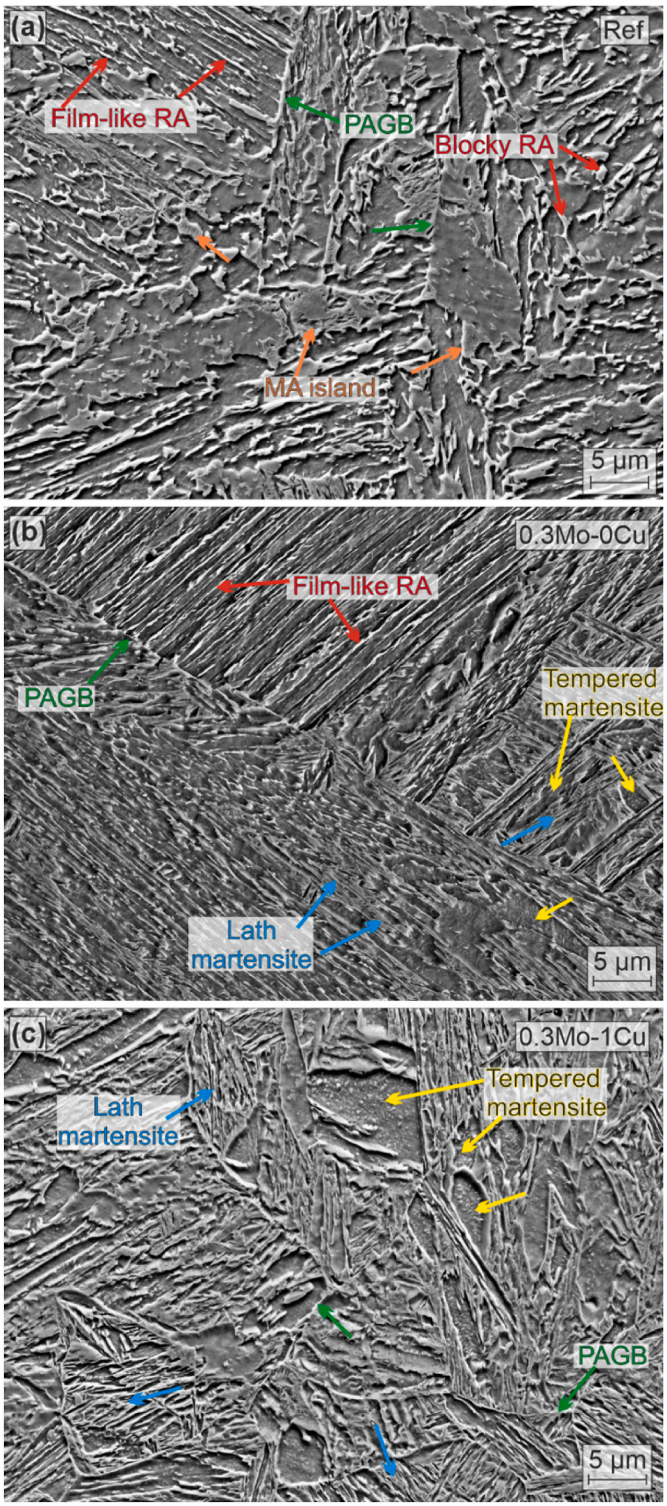


Fig. 2. Higher magnification SEM images of (a) Ref, (b) 0.3Mo-0Cu, and (c) 0.3Mo-1Cu steels, showing microstructural differences.

fraction strongly depends on the surface preparation as well as the particular measurement location within the microstructure. The free surface condition may reduce mechanical constraint during grinding and polishing and promote strain-induced martensitic transformation, leading to a limited RA measurement. In contrast, as XRD is a volumetric measurement technique, it is more suitable for the determination of RA fractions. The RA fractions obtained via EBSD and XRD are shown in Table 2. As expected, the RA fractions obtained via EBSD are lower than those measured by XRD. Among the three microstructures, the highest RA fraction, as determined by XRD, is obtained in Ref steel at 6.2%, followed by the 0.3Mo-0Cu with 5%, and 2.9% in the 0.3Mo-1Cu steel. In this respect, a clear trend can be identified, such that the RA fraction decreases with a decreasing bainite content. To further investigate the mechanical stability of RA, deformed specimens were also subjected to an additional XRD measurement after tensile testing. Due to specimen size restrictions, the measurements were performed approximately 10 mm from the fracture surface. The measured RA fractions after deformation was measured as 0.3%, 1.6%, and 0% for the Ref, 0.3Mo–0Cu, and 0.3Mo–1Cu steels, respectively, showing a substantial decrease tensile loading (cf. Table 2).

In addition to the microstructural differences, notable variations are observed in the PAG size of the investigated steels, particularly for 0.3Mo-1Cu steel. To visualize the PAGs, a low-magnification EBSD mapping was employed and PAGs were reconstructed via post-processing. As shown in Fig. 3, PAG size of the Ref and 0.3Mo-0Cu steels were relatively large, whereas 0.3Mo-1Cu steel has significantly smaller PAG size with further Cu alloying. Quantitative analysis confirmed the EBSD observation, exhibiting average PAG size of 148 μm, 124 μm and 45 μm for the Ref, 0.3Mo-0Cu and 0.3Mo-1Cu steels, respectively. Fig. 3d shows the statistical distribution of the measured PAG size of the investigated steels. These findings are particularly noteworthy, as they suggest a pronounced influence of Cu addition on austenite grain growth after forging.

3.2. Mechanical properties

An overview of the mechanical properties obtained from tensile tests, hardness measurements, and V-notch Charpy impact tests is summarized in Table 3. The engineering stress-strain curves obtained from tensile tests are represented in Fig. 4a. As shown in Fig. 4a, the stress-strain curve of all studied steels displays continuous yielding behavior and uniform plastic deformation. The yield strength (YS) and ultimate tensile strength (UTS) range from 753 to 900 MPa and 1157 to 1407 MPa, respectively. The Ref steel exhibits the lowest YS at 753 MPa, while the 0.3Mo-1Cu shows the highest at 900 MPa. A similar trend is observed for UTS, with Ref material reaching 1157 MPa, and the 0.3Mo-1Cu shows the highest at 1400 MPa. The obtained strength values are also reflected in the hardness of the investigated steels. The Ref steel exhibits the lowest hardness at 396 HV10, which increases to 418 HV10 in the 0.3Mo-0Cu, and reaches the highest value of 443 HV10 in the 0.3Mo-1Cu steel (cf. Table 3). In contrast, the achieved tensile elongations display a different pattern. The 0.3Mo-0Cu steel exhibits the lowest uniform elongation (UE) and total elongation (TE), at 4.1% and 9.5%, respectively. Whereas the Ref steel shows the highest ductility, with 6.7% UE and 15% TE, while the 0.3Mo-1Cu steel shows intermediate elongation values of 4.8% UE and 12.6% TE.

Table 2
Retained austenite fractions obtained via EBSD and XRD.

Steel	Undeformed condition			Deformed condition
	RA fraction (%) (low-mag. EBSD)	RA fraction (%) (high-mag. ROI-EBSD)	RA fraction (%) ± 2 (XRD)	RA fraction (%) ± 2 (XRD)
Ref	2.1	3.8	6.2	0.3
0.3Mo-0Cu	0.4	1.1	5	1.6
0.3Mo-1Cu	0.3	1.8	2.9	0

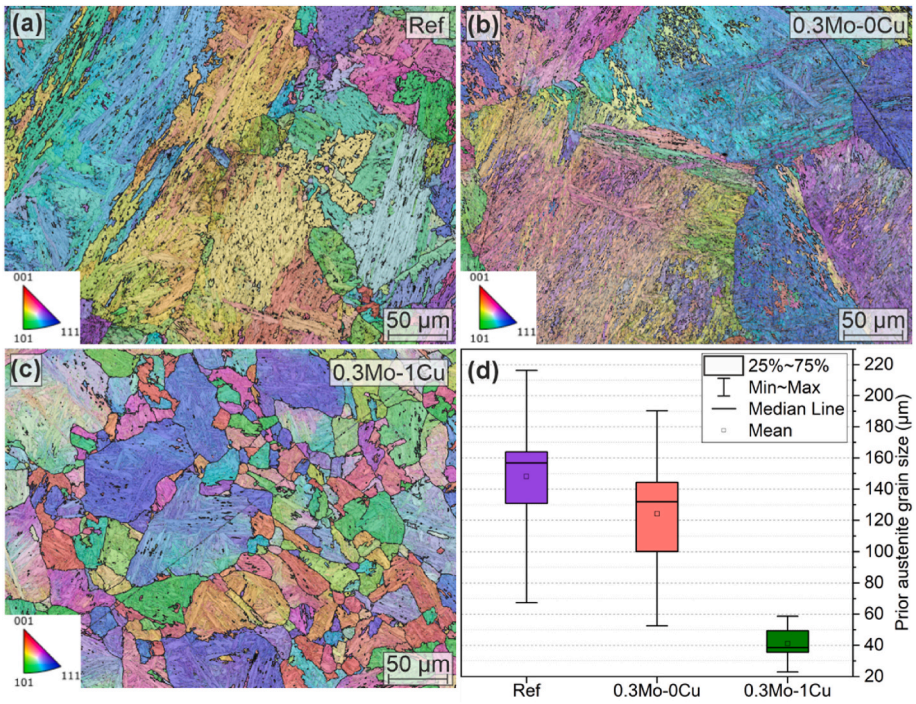


Fig. 3. EBSD-IPF maps superimposed with band contrast maps showing the reconstructed prior austenite grains of (a) Ref, (b) 0.3Mo-0Cu, and (c) 0.3Mo-1Cu steels. (d) Statistical distribution of the measured PAG size of the investigated steels showing the minimum and maximum, mean, median, and interquartile range (25th-75th percentile).

Table 3
Mechanical properties obtained from tensile tests, hardness measurements, and V-notch Charpy impact tests along with formability index (FI) and strength-toughness index (STI).

Steel	YS (MPa)	UTS (MPa)	UE (%)	TE (%)	Hardness (HV10)	Impact En. (J)	FI (MPa•%)	STI (MPa•J)
Ref	753 ∓ 33	1157 ∓ 13	6.7 ∓ 0.6	15.0 ∓ 0.9	396 ∓ 8	21 ∓ 5	7752	15813
0.3Mo-0Cu	879 ∓ 1	1323 ∓ 13	4.1 ∓ 0.3	9.5 ∓ 1.7	418 ∓ 21	48 ∓ 9	5424	42192
0.3Mo-1Cu	900 ∓ 8	1407 ∓ 11	4.8 ∓ 0.1	12.6 ∓ 0.6	443 ∓ 12	51 ∓ 3	6754	45900

Regarding the impact toughness, while the Ref steel exhibits the lowest impact toughness by 21 J, the 0.3Mo-0Cu and 0.3Mo-1Cu show a similar toughness by 48 J and 51 J, respectively. However, it is important to note that the 0.3Mo-0Cu steel displays the highest scattering in the results of hardness and Charpy impact tests (cf. Table 3). This was also reflected in the instrumented Charpy force–displacement curves (Fig. 4b), revealing the distinct differences in impact toughness behavior among the investigated steels. The Ref steel exhibits the lowest peak force (17.3 kN) and the shortest total displacement, indicating early fracture and limited plastic deformation. With Mo addition in the 0.3Mo–0Cu, both the maximum force (25.5 kN) and total energy increase, reflecting improved crack resistance. The 0.3Mo-1Cu alloy shows the highest peak load (29.3 kN) and the largest area under the curve, corresponding to enhanced impact toughness and a more stable crack propagation behavior.

Additionally, the formability index (FI) is calculated, which is a product of UTS and UE (cf. Table 3), provides an additional measure of material's ability to sustain high stresses while accommodating uniform plastic deformation before localization occurs. Correspondingly, it is used as an indicator for the balance between strength and formability, particularly in sheet applications. On the other hand, forgings are typically designed to have high YS and impact toughness, as they reflect load-carrying capacity and resistance against impact, respectively. Therefore, a strength-toughness index (STI) is introduced in this study as a product of YS and Charpy impact energy to be able to compare investigated steels in terms of their forging-relevant mechanical performance. In Fig. 4c, the FI and STI of the investigated steels are presented together with impact toughness and hardness values. Compared to the Ref Steel, with Mo alloying in the 0.3Mo-0Cu, a pronounced increase in hardness and impact toughness is obtained; however, this increase is accompanied by a notable drop in FI from 7752 MPa•% to 5424 MPa•%. On the other hand, the STI increases substantially from 15813 MPa•J to 42192 MPa•J. Interestingly, with further Cu alloying in the 0.3Mo-1Cu, the FI improves again to 6754 MPa·%, while exhibiting the highest hardness and impact toughness among the investigated steels. In addition, the STI further increases to 45900 MPa•J, representing highest strength-toughness balance amongst the steels investigated.

The differences in impact toughness of the steels are consistent with the fracture surface morphologies shown in Fig. 5. The macroscopic fracture features show that the Ref steel has the smallest shear lip area at the edges of the specimen, while the 0.3Mo-1Cu has the largest area (cf. Fig. 5a–c). Microscopic investigations reveal that the fracture surface of the Ref steel is dominated by brittle fracture characteristics, consisting mainly of intergranular and cleavage fracture with only minimal dimple regions (cf. Fig. 5d–g). In the case of 0.3Mo-0Cu steel, almost no intergranular fracture is observed, while the fraction of ductile regions is notably increased (cf.Fig. 5e–h). In 0.3Mo-1Cu steel, the fracture surface consists predominantly of ductile fracture characteristics revealed by dimple regions along with cleavage fracture features (cf. Fig. 5f–i). However, the cleavage facets in 0.3Mo-0Cu are noticeably larger than those observed in the 0.3Mo-1Cu steel, as shown in Fig. 5h–i,

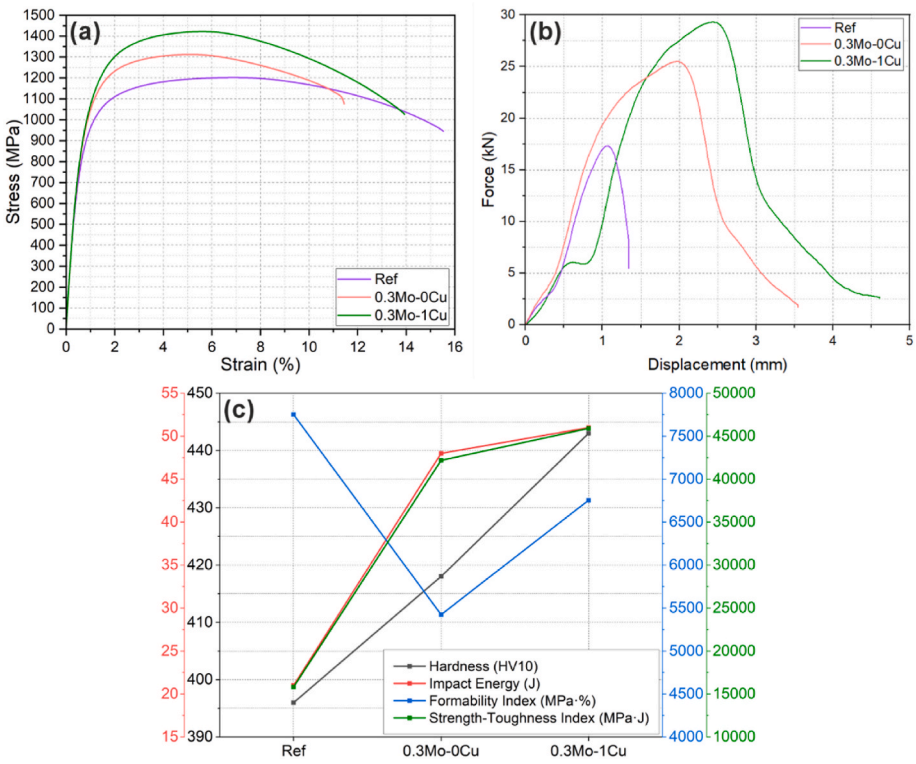


Fig. 4. (a) Engineering stress-strain curves, (b) force-displacement curves from instrumented Charpy impact tests, and (c) comparison of the hardness, impact energy, formability index, and strength-toughness index of the studied steels.

respectively.

The LIT approach is employed to provide additional industrial relevance as it provides a time- and cost-efficient assessment of fatigue performance with a single specimen test [23–25,27–29]. Fig. 6 shows the evolution of the surface temperature as a function of increasing stress amplitude during LIT for the investigated steels. In all cases, the surface temperature rises gradually with increasing stress amplitude and number of cycles. A steady temperature increase of 0.1 – 0.5 °C per million cycles is observed in all steels up to a certain stress amplitude, after which a pronounced and sudden jump occurs. For the Ref and 0.3Mo–0Cu steels, the sharp temperature increase is observed at a stress amplitude of 450 MPa, whereas for the 0.3Mo–1Cu steel, this occurs at a considerably higher stress amplitude of 580 MPa.

4. Discussion

Microstructural investigations reveal a progressive decrease in the bainite fraction and a corresponding increase in martensite content with Mo and Mo-Cu alloying, as respectively shown in Fig. 1a–c. This explains the difference between the RA fractions in the final microstructures. As all alloys are alloyed with sufficient amounts of Si and Al in total, the carbide precipitation during bainitic transformation is suppressed [30,31]. This leads to carbon enrichment in the surrounding austenite and to the formation of carbide-free bainite (CFB) in the Ref and 0.3Mo-0Cu steels. Since the Ref steel exhibits the highest bainite fraction, it consequently contains the largest amount of RA in the final microstructure. Resultingly, the lower bainite fraction in the 0.3Mo-0Cu steel is accompanied by a corresponding decrease in RA. Accordingly, the 0.3Mo-1Cu steel has the lowest retained austenite fraction, which has not gone through bainitic transformation, implying limited carbon enrichment in the retained austenite.

It is well-known that Mo is widely used to retard the diffusional phase transformations, such as ferritic and pearlitic [32,33]. This is mainly due to its tendency to segregate at austenite grain boundaries [34,35], where it occupies potential nucleation sites, leading to a delay in ferrite formation, thus enhancing the hardenability [36]. However, although several studies have reported that Mo alloying has a similar effect on bainite transformation kinetics as on diffusional transformation products due to the same reasons [37], the influence of Mo on bainite formation kinetics is rather complex [38,39]. In bainitic transformation, even though there is carbon partitioning, the formation of BF is diffusionless, as in martensitic transformation. Therefore, the influence of Mo alloying is not straightforward on bainite transformation kinetics, owing to the complex nature of the bainitic transformation. It has been reported that Mo segregation on PAGBs leads to lower grain boundary energy [40], which can slow down the nucleation rates of all ferrite products [40,41]. Moreover, Kong et al. [42] studied the influence of Mo on bainite transformation during continuous cooling in low-carbon micro-alloyed steel and showed that 0.4 wt% Mo slows down the bainite transformation relative to the Mo-free variant. This retardation in bainite transformation was attributed to the strong carbide-forming effect of Mo as it increases the activation energy for carbon diffusion in austenite and, correspondingly, lowers the carbon diffusion coefficient. Since bainite formation involves carbon redistribution, the reduced carbon mobility slows down the overall transformation kinetics. Additionally, Mn, which shows a strong tendency to segregate to PAGBs, may lead to compositional heterogeneities that can influence bainitic transformation behavior. Owing to its stronger grain-boundary affinity of Mo, compared to Mn, it preferentially occupies the PAGBs and may suppress Mn enrichment at these sites [34,36]. Speculatively, this could result in a more homogeneous Mn distribution in austenite rather than on PAGBs, reducing the local heterogeneities and indirectly improving the chemical stability of austenite against bainitic transformation. However, a definitive confirmation of this mechanism requires dedicated and detailed atomic-scale characterization of the elemental distribution at PAGBs and their surroundings.

Nevertheless, the obtained results show that the Mo alloying at rather high concentrations delays the bainitic transformation and

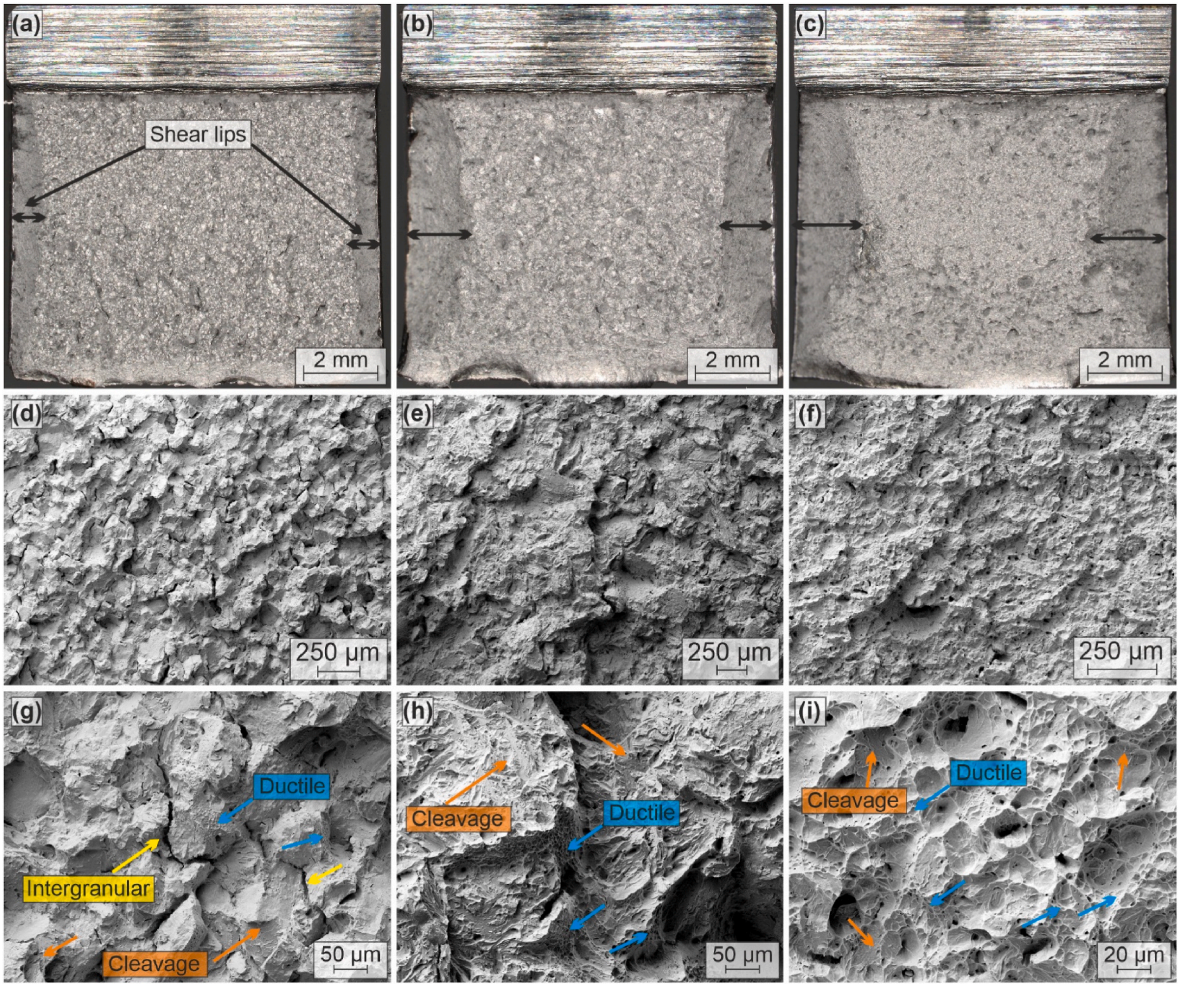


Fig. 5. Fracture surfaces of the (a, d, g) Ref, (b, e, h) 0.3Mo–0Cu, and (c, f, i) 0.3Mo–1Cu steels after Charpy impact testing, showing the macroscopic (a–c) and microscopic (d–i) fracture features.

increases the critical cooling rate to form martensite, promoting martensitic transformation during air cooling (cf. Fig. 1). This is supported by dilatometric experiments conducted at a 0.1 K/s cooling rate, representing air-cooling. Fig. 7a shows the dilatation curves, displaying bainitic and martensitic transformation ranges of the investigated steels. As highlighted with an arrow, in the Ref steel, there is a clear bainitic transformation overlapping with martensitic transformation during continuous cooling. This is further confirmed by the first derivative of the dilatation curves in Fig. 7b, where two distinct peaks with maxima at ~390 °C and ~290 °C can be clearly seen for the Ref steel, which are corresponding to the temperatures of maximum transformation rate for the bainitic and martensitic transformations, respectively. In contrast, with Mo alloying in 0.3Mo-0Cu steel, while no clear bainitic transformation was observed in the raw dilatation curve (cf. Fig. 7a), the corresponding derivative shows two peaks, however more closely overlapped, that cannot be observed in the raw data (cf. Fig. 7b). The first peak with its maximum at ~370 °C is shifted to a lower temperature and reduced in intensity compared to the Ref steel, indicating that the bainitic transformation is not absent but rather delayed and takes place with a slower transformation rate, consistent with Mo-induced retardation of bainitic transformation. The second peak at ~330 °C corresponds to martensitic transformation. The close overlap between the two peaks explains why the bainitic transformation appears to be absent in the raw dilatation curve. Additionally, the progressive retardation of bainitic transformation observed in air-cooled microstructures (cf. Fig. 1), confirmed by the dilatometric analysis, is further supported via thermodynamic calculations of the driving force for bainite nucleation using the model proposed by Bhadeshia [43]. The calculations, shown in Fig. 7c, show a progressive reduction in the driving force for bainite nucleation with Mo alloying, which provides a thermodynamic support for the experimentally observed retardation in the 0.3Mo-0Cu steel.

Furthermore, the microstructural observations reveal that the 0.3Mo-0Cu steel exhibits a visibly finer CFB microstructure and significantly minimized MA island formation on PAGBs compared to the Ref steel (cf.Fig. 2). It has been reported that Mo addition, particularly at higher concentrations, has a refining influence on bainite and MA structures [41,42,44,45]. Kong et al. [42] attributed this microstructural refinement also to the restraining effect of Mo on carbon diffusivity in austenite. The suppressed carbon mobility has a kinetic consequence, similar to that of an increased cooling rate, with comparable refining effects on the final microstructure.

With further Cu alloying in 0.3Mo-1Cu steel, the bainite formation is fully suppressed, and a fully martensitic microstructure is achieved via air cooling (cf.Fig. 1c). This is also consistent with the corresponding dilatation curve in Fig. 7a, where no visible bainitic transformation is observed. The first derivative of the dilatation curve further confirms this transformation behavior by displaying a single peak with a maximum at ~320 °C (cf.Fig. 7b), also confirm that there was no detectable bainitic transformation. These findings are also consistent with the thermodynamic calculations, where 0.3Mo-1Cu steel exhibits the lowest driving force for bainite nucleation among the investigated steels, supporting the complete suppression of the bainitic

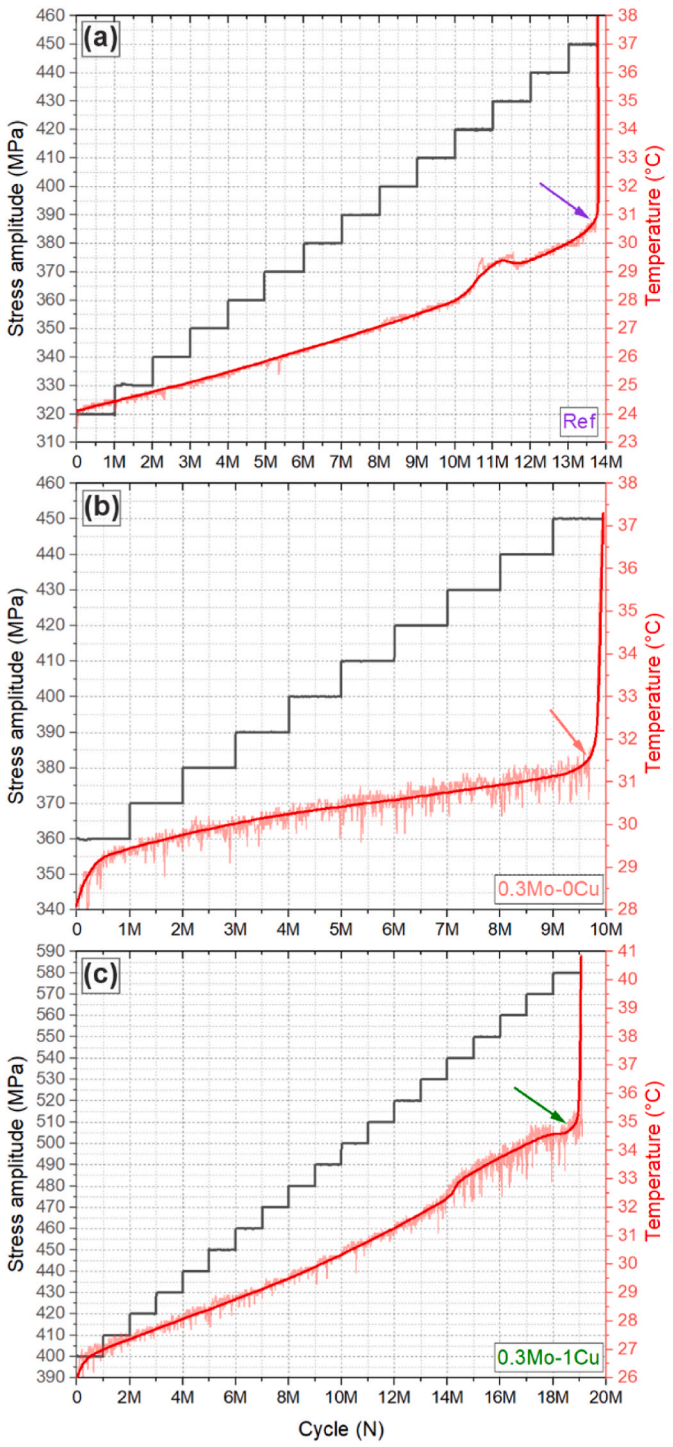


Fig. 6. Load increase test of the (a) Ref, (b) 0.3Mo-0Cu, and (c) 0.3Mo-1Cu under high-frequency (1 kHz) cyclic loading, showing temperature evolution during successive 10 MPa stress amplitude increments.

transformation with additional Cu alloying. While Mn and C are well-known to be stronger austenite stabilizers, Cu has also been reported to enhance the thermal stability of austenite [46], which suppresses bainitic transformation, leading to improved hardenability. This behavior was demonstrated and further supported in a previous dilatometric study conducted on the same alloy class [16], where Cu addition was shown to lower martensite start temperature and to fully suppress bainitic transformation even under very slow cooling conditions (0.05 °C/s). A similar trend has also been reported in another study conducted on Cu-modified 42CrMo4 QT steel [15], where increasing Cu content progressively shifted the bainite transformation bay to slower cooling rates on continuous-cooling-transformation (CCT) diagrams and reduced the critical cooling rate to achieve fully martensitic microstructure from 6.25 K/s to 1.5 K/s. These consistent observations across different alloy systems support the general nature of the Cu-induced retardation of bainite transformation during continuous cooling. Beyond this, the positive effect of Cu on the mechanical stability of RA and the resulting mechanical properties has been reported by Ding et al. [19]. This effect was attributed to the presence of Cu-rich nanoparticles, which act as obstacles to dislocation motion, thereby strengthening the austenite. Additionally, these nanoparticles hinder the migration of phase boundaries, which in turn promotes an increased partitioning of Mn into the austenite.

As shown in Fig. 3, the 0.3Mo-1Cu steel exhibits significantly smaller PAGs compared to the other two steels, indicating that Cu alloying effectively controls the austenite grain growth after forging. It is known that solute atoms or precipitates can delay the movement of dislocations, grain boundaries, and phase boundaries due to pinning or the solute drag effect (SDE) [47]. Several studies have reported Cu as an effective element to control PAG size [46,48–51]. Antonione et al. [49] showed the ability of Cu to effectively delay recrystallization through SDE, even in the absence of Cu-precipitates. A similar influence of Cu on austenite grain size control in high-Mn steels (31 wt% Mn) has been reported by Tong et al. [18], who demonstrated that a 3 wt% Cu addition effectively inhibits austenite grain growth, when the solution treatment temperature is increased from 950 °C to 1050 °C. This resulted in enhanced grain boundary strengthening, attributed to the fine grain size arising from Cu-mediated grain growth inhibition. In another study conducted by Duan et al. [52], a solute drag model was applied to derive the segregation energy of Cu using experimental data obtained from plain C-Mn steel with varying Cu concentrations and at different temperatures, which was then used to predict the potential retardation of grain boundary motion in the presence of Cu solutes. The results confirmed that Cu effectively suppresses the austenite grain growth by inducing a measurable SDE on migrating grain boundaries.

With Mo and Mo-Cu alloying, a clear increasing trend is observed in the hardness, YS, and UTS of the investigated steels, respectively (cf. Table 3 and Fig. 4a). The increase in strength can be primarily attributed to the increased martensite fraction, which is inherently a harder and stronger phase than bainite. In addition, the reduced fraction of RA with Mo and Mo-Cu alloying is expected to contribute to the obtained increase in YS, as RA is comparatively a softer phase due to its crystal structure that promotes early yielding. Conversely, RA may increase the UTS through strain-induced martensitic transformation during plastic deformation. Consequently, it can be deduced that the overall strength of the studied steels is governed by the relative proportion of martensite in the microstructure. In addition to microstructural differences, solid-solution strengthening through Mo and Mo-Cu alloying is another factor that enhances the matrix strength of individual phases [53,54], the contribution of Mo and Cu to the solid solution strengthening can be estimated using equation (1):

$$\sigma_{ss} = 32Mn + 678P + 83Si + 39Cu - 31Cr + 11M \quad (1)$$

demonstrating that the increase of the yield strength by solid solution strengthening for alloys 0.3Mo-0Cu and 0.3Mo-1Cu is limited to 3.3 MPa as well as 42.3 MPa, respectively. As the real differences in YS to the Ref alloy are 126 and 147 MPa, the dominating factor is the increasing share of martensite volume fraction.

While strength increases with the martensite fraction, UE and TE tend to decrease, reflecting the typical strength-ductility trade-off between the hard martensitic microstructure and the relatively ductile CFB. The face-centered cubic (FCC) RA phase present in CFB can facilitate more dislocation motion compared to the body-centered cubic (BCC) phases, which enhances the plasticity during tensile deformation. Additionally, improved tensile elongation of CFB microstructures due to

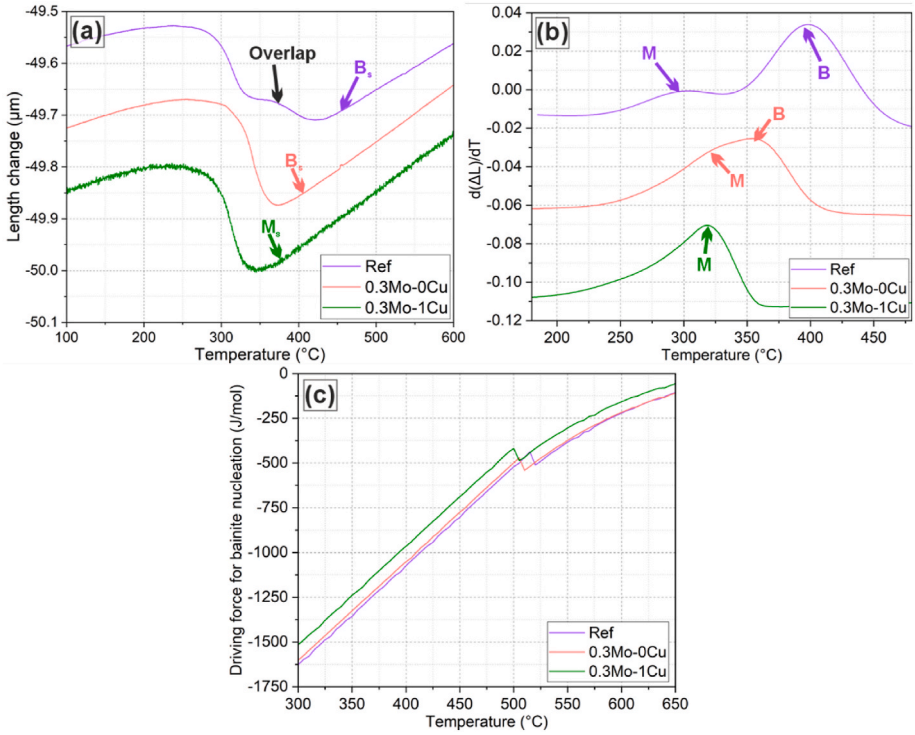


Fig. 7. (a) Dilatation curves displaying bainitic and martensitic transformation range during continuous cooling at 0.1 K/s, representing air cooling. (b) Rate of dimensional change as a function of temperature (first derivative of the dilatation curves in (a). (c) Driving force for bainite nucleation calculated using Bhadeshia's model [43].

the gradual transformation of metastable RA to martensite through transformation-induced plasticity (TRIP) is a very well-known phenomenon [25,55]. This interpretation is further supported by additional XRD measurements on the deformed specimens after tensile testing, exhibiting pronounced reduction in RA observed in all three steels (cf. Table 2). This confirms that a substantial amount of RA underwent strain-induced transformation to martensite during tensile loading. Therefore, the Ref steel, containing the largest amount of bainite and RA, shows the highest UE and TE compared to the martensite-rich variants. In this context, both UE and TE slightly decrease in the fully martensitic 0.3Mo-1Cu alloy compared to the Ref steel (cf. Table 3 and Fig. 4a). However, interestingly, the 0.3Mo-0Cu steel exhibits the lowest tensile elongation values (cf. Table 3 and Fig. 4a), although it still contains a considerable amount of bainite. The overall results suggest that the ductility is governed by a delicate balance between the amount of bainite, relatedly RA, and martensite in the microstructure, which is in turn influenced by alloying-induced phase transformation kinetics. It can be deduced that multiple deformation mechanisms act simultaneously, and their relative dominance is determined by the prevailing microstructure. In the Ref steel, the tensile deformation behavior is mainly governed by the bainitic matrix and the gradual transformation of RA to martensite. The 0.3Mo–1Cu steel, characterized by a fully martensitic microstructure, benefits from the auto-tempered martensite, improving the strength significantly without a distinct loss of ductility. In contrast, the elongation behavior of a balanced bainite/martensite containing 0.3Mo–0Cu steel indicates that the beneficial effects of both ductility-enhancing mechanisms are less effective when neither phase is predominant. Overall, these findings strongly emphasize that an optimized strength-ductility balance in such complex steels requires an optimized interplay amongst bainite transformation, RA fraction and stability, and martensite.

While the near-complete depletion of RA after tensile testing in all three steels (cf. Table 2) confirms that strain-induced transformation was active in every case, the ductility cannot be rationalized solely on the basis of the RA fraction; its mechanical stability must be taken into account. In the case of the investigated steels, this stability is mainly governed by the carbon enrichment of the RA, which in turn depends on the extent of bainitic transformation. In the Ref steel, the high fraction of bainitic transformation promotes more carbon partitioning from the formed bainitic ferrite to surrounding austenite compared to the other steel states. Consequently, the carbon-enriched RA becomes more mechanically stable, offering enhanced resistance to strain-induced transformation, so that the TRIP effect persists to higher strains before localization occurs, contributing to the highest uniform and total elongation. With Mo alloying in the 0.3Mo-0Cu steel, the bainitic transformation is partially suppressed, reducing carbon partitioning into the austenite, lowering its mechanical stability. The less stable RA transforms faster, which results in weakened TRIP contribution causing decreased tensile ductility. However, it must be noted that the reduced RA fraction and stability could be only one of the factors contributing to the loss of ductility in the 0.3Mo-0Cu steel, as the microstructure consists of a balanced combination of bainite and martensite. If the ductility were governed by the RA fraction alone, the elongation would follow the order of the measured RA contents (Ref $>$ 0.3Mo-0Cu $>$ 0.3Mo-1Cu). This is, however, not observed as the auto-tempered martensitic 0.3Mo-1Cu steel shows improved elongation compared to the 0.3Mo-0Cu steel despite its minimal RA fraction and little to no carbon enrichment as it does not undergo bainitic transformation, meaning no improvement in the mechanical stability of RA. Instead, the tensile elongation is mainly carried by the homogeneous auto-tempered martensite, as mentioned, which highlights the importance of microstructural homogeneity for the ductility of such complex steels.

Although the Ref steel exhibits the highest tensile elongation, it shows the lowest impact toughness among the investigated steels. This suggests that the change in deformation mechanism alters the mechanical response of microstructural constituents, as well as the fracture behavior. During tensile testing, the gradual transformation of RA to martensite improves the total elongation through the TRIP effect [56].

However, fracture surface analysis reveals intergranular fracture as the dominant feature after impact testing (cf. Fig. 5g), indicating weakened PAGBs. Previous studies have reported that the MA constituents and RA located at PAGBs tend to deteriorate impact toughness [55,57,58]. The sudden transformation of RA to martensite, together with the presence of inherently brittle MA islands, particularly along PAGBs, might have locally promoted a brittle network along the PAGBs during impact loading. Furthermore, Du et al. [59] mentioned that impact toughness is more susceptible to heterogeneities among the mechanical properties of each microstructural constituent than its tensile properties. It was highlighted that the deformation incompatibility between RA and tempered martensite increases the stress concentration at the interface of the constituent phases, leading to microcrack formation and deterioration in impact toughness. In addition to that, Mn segregation on PAGBs, as a common phenomenon in medium-Mn steels [12], has been reported to reduce the cohesive strength of these boundaries [11], facilitating intergranular fracture. The impact toughness results for the 0.3Mo–0Cu steel support these findings, as it exhibits notably higher impact toughness and predominantly transgranular fracture characteristics, with ductile dimples on the fracture surface. With Mo alloying, the bainite fraction decreases along with the RA. It is also observed that the MA constituents in the vicinity of PAGBs are reduced (cf. Fig. 2). Furthermore, Mo alloying has been proven to be an effective strategy to improve the grain boundary cohesion [34] and, consequently, the impact toughness [13], primarily through suppression of Mn segregation at PAGBs. The 0.3Mo–1Cu steel, characterized by a fully martensitic microstructure, shows the highest impact toughness with minimal deviation among the investigated steels (cf. Table 3), despite exhibiting the highest strength. This behavior can be attributed to the homogeneous auto-tempered microstructure, unlike the other investigated steels, which promotes uniform stress distribution and reduces the possibility of premature crack initiation. This is also indicated in the EBSD-KAM maps of the investigated steels acquired from the ROIs shown Fig. 8, where the 0.3Mo–1Cu (cf. Fig. 8c), showing the most homogeneous distribution of local misorientation compared to other investigated steels. The presence of auto-tempered martensite further enhances toughness by relieving local stresses and enabling plasticity, which is commonly observed in QT steels [60,61]. Moreover, 0.3Mo–1Cu steel exhibits a significantly smaller PAG size (cf. Fig. 3), resulting in an increased number of high-angle boundaries, consequently providing more efficient barriers to crack propagation under dynamic loading. This is also reflected in the fracture surface obtained after impact testing, where the cleavage facets are significantly smaller compared to the other steels, indicating the influence of smaller PAG size. As Cu alloying is shown to be an effective method to control the PAG size, its positive influence on boundary cohesion may further contribute to the improved impact toughness under dynamic loading. The combined effects of Mo and Cu, which improve boundary cohesion and matrix toughness and promote a homogeneous auto-tempered martensitic microstructure through air cooling, result in a more stable crack propagation behavior and the highest absorbed impact energy among the investigated steels.

The LIT results clearly distinguish the fatigue performance of the 0.3Mo–1Cu steel from that of the other two investigated conditions. The 0.3Mo–1Cu steel, which exhibits the highest UTS under quasi-static loading (cf.Table 3 and Fig. 4a), also shows the highest stress amplitude at 580 MPa as the onset of the abnormal temperature rise during LIT (cf. Fig. 6). This behavior is consistent with the underlying principle of the LIT approach, whereby cyclic plastic deformation is accompanied by energy dissipation manifesting as a measurable thermal response at the specimen surface, such that a sudden and pronounced temperature rise can be directly associated with the onset of fatigue-relevant damage [27]. This indicates a significantly higher fatigue limit and confirms its superior resistance against cyclic loading and crack initiation in comparison to the Ref and 0.3Mo-0Cu, both of which show the abnormal temperature rise at 450 MPa (cf. Fig. 6). Previous studies have shown that phase boundaries in multi-phase microstructures are commonly identified as the preferred sites of stain localization under cyclic loading, where local cyclic deformation in the softer phase leads to crack initiation [62,63]. This behavior can also be correlated with EBSD-KAM maps in Fig. 8. While 0.3Mo–1Cu steel exhibits a comparatively uniform local misorientation distribution (cf. Fig. 8c), the Ref and 0.3Mo-0Cu conditions reveal heterogeneities, particularly between

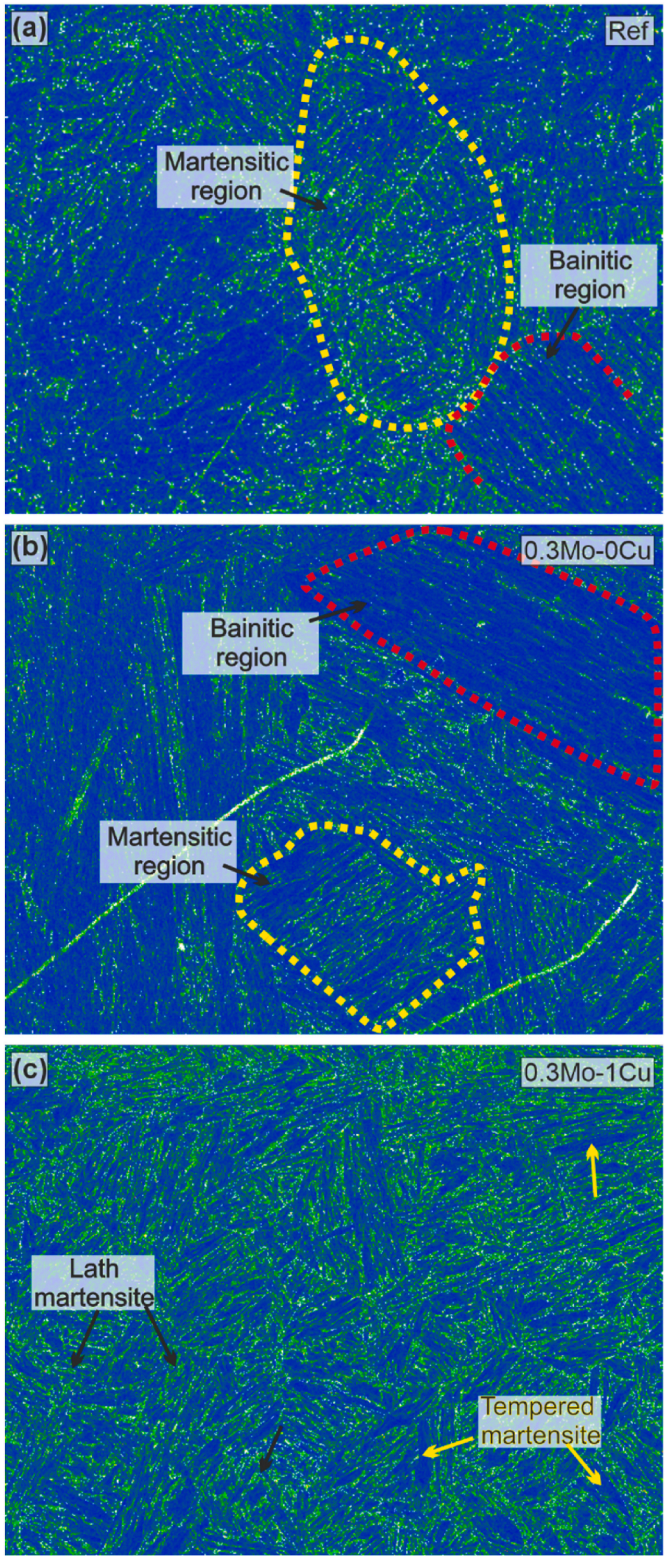


Fig. 8. EBSD-KAM maps of (a) Ref, (b) 0.3Mo-0Cu, and (c) 0.3Mo-1Cu steels showing the local misorientation distribution within the selected ROIs.

martensitic and bainitic regions, as highlighted in Fig. 8a–b. These local misorientation gradients and associated transitions may promote local strain incompatibilities under cyclic loading. Consequently, such incompatibilities can lead to localized stress concentrations, acting as microstructural stress raisers and promoting earlier crack initiation. Cheng et al. [64] demonstrated such mechanism in a bainite-martensite dual-phase steel, where a greater strain accumulation was preferentially observed in bainite and persistent slip bands (PSB) formed at the bainitic ferrite-martensite interfaces, acting as crack initiation sites.

Beyond the incompatibilities between bainitic and martensitic regions, the specific phase morphologies further influence the crack initiation under cyclic loading. Gao et al. [65] demonstrated that the RA morphology play a significant role in fatigue crack initiation in bainitic steels. It was shown that the film-like RA between BF plates arrest small crack growth by transforming at the crack tip, while blocky RA and MA islands, especially the ones along the PAGBs, promote intergranular crack initiation as a result of ease of slip activation in RA. In this respect, the coexistence of RA, BF, MA constituents, and both lath and auto-tempered martensite in the Ref and 0.3Mo-0Cu steels introduces additional mechanical incompatibilities between constituents of differing hardness and deformation behavior, increasing the number of further potential sites for local strain localization and crack initiation under cyclic loading. On the other hand, the 0.3Mo-1Cu steel is essentially free of blocky retained austenite and MA islands and consists of a homogeneous auto-tempered martensitic matrix, which, together with its markedly finer prior austenite grain size promotes a more uniform accommodation of cyclic microplasticity and improves the resistance against the early growth of microstructurally short fatigue cracks.

The gradual temperature increase monitored in all steels during the majority of the tests can be attributed to the high-frequency loading conditions (1 kHz), which cause continuous mechanical energy dissipation as heat. This reflects the thermal response of the specimens rather than fatigue damage accumulation, as the temperature increase remains quite stable and smooth until the temperature jumps. Only the abrupt and pronounced temperature change can be correlated with the fatigue damage. On the other hand, the Ref and 0.3Mo-1Cu steels show irregularities in the temperature evolution before the final jump occurs (cf. Fig. 6a–c). These fluctuations may indicate the onset of early fatigue damage; however, this interpretation remains uncertain, as such deviations could also be a measurement-related artefact. Therefore, no definitive conclusion can be drawn regarding their origin. Nevertheless, these deviations do not influence the overall outcome, as the 0.3Mo-1Cu steel clearly exhibits the highest fatigue resistance in the LIT framework. However, it should also be acknowledged that in high-frequency LIT-based fatigue assessment, the progressive cyclic stress history may introduce pre-fatigue effects, whereby cumulative damage accumulated during the early loading stages could potentially influence the measured fatigue response. Correspondingly, the estimated fatigue limit may deviate from the intrinsic material fatigue limit [66,67]. On the other hand, several considerations support the reliability of the results obtained in this study. As established in a prior study on bainitic steels [25], conducted with the same methodology and testing equipment, demonstrated promising agreement between LIT-derived fatigue limit estimates and those determined via the staircase method across four different bainite groups, suggesting that pre-fatigue effects do not significantly distort the comparative outcome for this class of steels. Moreover, since the primary purpose of the LITs in this study is comparative rather than absolute, any systematic pre-fatigue effect would be expected to affect all investigated alloy conditions in a similar manner, preserving the relative ranking of fatigue performance amongst the steel variants. Therefore, while the absolute values of the estimated fatigue limits should be interpreted with appropriate caution, the comparative conclusions drawn from the LIT results are considered reliable within the scope of this study.

While the main scope of this study is to investigate the effect of Cu on the microstructure evolution and the resulting mechanical properties, naturally the question arises if critical embrittlement or hot shortness was observed. While the hot forming was performed in the critical temperature region for hot shortness (>1100 °C), no critical embrittlement was observed, and the ingot were forged with similar surface qualities as the two other melts. The resilience of the alloys investigated against Cu induced hot shortness could be explained by a variety of reasons. As the embrittlement by Cu is a combined process of selective oxidation and liquid metal embrittlement, the chemical composition of the grain boundary is of importance. As Mn is also known to enrich at PAGBs [10], interactions with Cu can be expected, especially as the Mn concentrations are much higher in comparison to low-alloyed steels, where the Cu embrittlement is most critical. Additionally, it was reported that Si alloyed steels are more resilient to Cu embrittlement as the oxidation mechanism fundamentally changes due to the formation of fayalite, which interacts with the Cu as well [68], which might increase the resistance against hot shortness.

5. Conclusion

As the global steel industry is increasing the usage of recycled steel during steel production, new alloying concepts need to be tested regarding their robustness against higher degrees of impurities. For this matter, a relatively lean variant of the recently developed air-hardening ductile forging steels was investigated regarding the effect of higher concentrations of Mo as well as Cu. From the investigations, the following conclusions can be drawn.

- Both Mo as well as Cu additions increase the hardenability of AHD steels, hence increasing the maximum thickness of forging components that can be produced via cost- and energy-efficient air hardening route, reducing the dependency on energy-intensive quenching and tempering processes.
- The addition of Cu leads to a pronounced reduction of the prior austenite grain size. While the Ref and 0.3Mo-0Cu steels exhibit relatively large average grain sizes of 148 µm and 124 µm, respectively, the Cu addition in the 0.3Mo-1Cu reduces this value distinctly to 45 µm. While recrystallization still takes place homogenously, the grain growth after recrystallization is significantly reduced, most likely due to the solid drag effect of Cu in solid solution.
- Fully martensitic microstructures, as achieved in the 0.3Mo-1Cu variant, are most preferable in AHD steels, particularly for forging applications, as they combine the highest yield strength (900 MPa) and ultimate tensile strength (1407 MPa) along with the highest impact energy (51 J) and the highest fatigue resistance (580 MPa) under the load increase test framework among the investigated AHD variants. These improvements are achieved without a significant ductility trade-off, as the total elongation of 12.6% remains the second highest among the investigated steels, 2.4% below the Ref and 3.1% above 0.3Mo-0Cu steel.
- The general fracture mechanism under different loading conditions, particularly for multiphase microstructures consisting of bainite and martensite, needs further investigation, as the results of ductility and toughness are contradictory.

Based on these results, it can be concluded that further recycling-induced additions of Mo as well as Cu to existing AHD steels are not critical in terms of the final properties of the steels, if Cu-induced hot shortness during production can be prevented.

CRediT authorship contribution statement

Oguz Gulbay: Conceptualization, Data curation, Formal analysis, Investigation, Methodology, Visualization, Writing – original draft, Writing – review & editing. **Oyku Guner:** Formal analysis, Investigation, Methodology, Writing – review & editing. **Adam Skowronek:** Writing – review & editing. **Aleksandra Kozłowska:** Funding

acquisition, Writing – review & editing. **Adam Grajcar:** Funding acquisition, Writing – review & editing. **Ulrich Krupp:** Funding acquisition, Supervision, Writing – review & editing. **Alexander Gramlich:** Funding acquisition, Supervision, Writing – review & editing.

Declaration of competing interest

The authors declare that they have no known competing financial interests or personal relationships that could have appeared to influence the work reported in this paper.

Acknowledgements

The study was funded by the Deutsche Forschungsgemeinschaft (DFG, German Research Foundation) – 504849602 and by the National Science Centre, Poland under the OPUS call in the Weave programme, grant no. 2021/43/I/ST5/02658.

Data availability

Data will be made available on request.

References

[1] W. Bleck, M. Bambach, V. Wirths, A. Stieben, Microalloyed engineering steels with improved performance – an overview, HTM Journal of Heat Treatment and Materials 72 (2017) 346–354.
[2] A. Gramlich, W. Hagedorn, K. Greiff, U. Krupp, Air cooling martensites—the future of carbon neutral steel forgings? Adv. Eng. Mater. 25 (2023).
[3] F. Ridlo, B. Zhang, C. Akkus, O. Gulbay, A. Chakraborty, B. Hu, H. Luo, et al., Influence of aluminum on microstructure and mechanical properties of air-hardened medium manganese steel, steel research int. 96 (2025).
[4] A. Gramlich, A. Middleton, R. Schmidt, U. Krupp, On the influence of vanadium on air-hardening medium manganese steels for sustainable forging products, steel research int. 92 (2021).
[5] T. Schmiedl, A.R.M. Gramlich, S. Schönborn, T. Melz, Behavior of forging steels under cyclic Loading—The benefit of air-hardening martensites, steel research int 91 (2020).
[6] A. Gramlich, H. Schäfers, U. Krupp, Influence of alloying elements on the dynamic recrystallization of 4 wt.-% medium manganese steels, Materials 13 (2020).
[7] A. Gramlich, R. Lange, U. Zitz, K. Büßenschütt, Air-hardening die-forged con-Rods—Achievable mechanical properties of bainitic and martensitic concepts, Metals 12 (2022) 97.
[8] W. Hagedorn, A. Gramlich, K. Greiff, U. Krupp, Alloy and process design of forging steels for better environmental performance, Sustain. Mater. Technol. 34 (2022) e00509.
[9] Y. Ma, Medium-manganese steels processed by austenite-reverted-transformation annealing for automotive applications, Mater. Sci. Technol. 33 (2017) 1713–1727.
[10] M. Kuzmina, D. Ponge, D. Raabe, Grain boundary segregation engineering and austenite reversion turn embrittlement into toughness: example of a 9 wt.% medium Mn steel, Acta Mater. 86 (2015) 182–192.
[11] K.H. Kwon, I.-C. Yi, Y. Ha, K.-K. Um, J.-K. Choi, K. Hono, K. Oh-ishi, et al., Origin of intergranular fracture in martensitic 8Mn steel at cryogenic temperatures, Scr. Mater. 69 (2013) 420–423.
[12] M. Nasim, B.C. Edwards, E.A. Wilson, A study of grain boundary embrittlement in an Fe–8%Mn alloy, Mater. Sci. Eng., A 281 (2000) 56–67.
[13] A. Gramlich, T. Schmiedl, S. Schönborn, T. Melz, W. Bleck, Development of air-hardening martensitic forging steels, Mater. Sci. Eng., A 784 (2020) 139321.
[14] A. Gramlich, S. Shayan, N. Babaei, A. Klubakov, L. Patterer, U. Krupp, H. Springer, Recycling-induced copper contamination of a 42CrMo4 quench and tempering steel—scaling and susceptibility to hot shortness, steel research int (2025).
[15] A. Gramlich, T. Hinrichs, H. Springer, U. Krupp, Recycling-induced copper contamination of a 42CrMo4 quench and tempering steel: alterations in transformation behavior and mechanical properties, steel research int 94 (2023).
[16] A. Skowronek, T.H. Kori, A. Gramlich, O. Gulbay, U. Krupp, A. Grajcar, Thermodynamic-kinetic and dilatometric characterization of the influence of Mo and Cu additions on phase transition behavior in high-strength medium-Mn steels, J. Therm. Anal. Calorim. 150 (2025) 20001–20011.
[17] J.-G. Jung, M. Jung, S.-M. Lee, E. Shin, H.-C. Shin, Y. Lee, Cu precipitation kinetics during martensite tempering in a medium C steel, J. Alloys Compd. 553 (2013) 299–307.
[18] C. Tong, C. Shen, L. Zhang, Y. Qi, C. Zhang, S. Zheng, Effect of Cu addition on the microstructure and the mechanical properties of austenitic low-density steel, Mater. Charact. 234 (2026) 116185.
[19] F. Ding, Q. Guo, B. Hu, Y. Xu, W. Lai, C. Zhang, X. Jin, et al., Influences of Cu alloying on precipitation, austenitic reversion and mechanical properties of NiAl-strengthened medium-Mn steels, Acta Mater. 284 (2025) 120623.
[20] F. Zvavamwe, J. Pasco, M.-K. Paek, C. Aranas, Influence of molybdenum additions on the microstructural properties of medium-Mn steels, J. Mater. Res. Technol. 39 (2025) 2570–2580.
[21] P. Cheng, B. Hu, S.L. Liu, H. Guo, M. Enomoto, C.J. Shang, Influence of retained austenite and Cu precipitates on the mechanical properties of a cold-rolled and intercritically annealed medium Mn steel, Mater. Sci. Eng., A 746 (2019) 41–49.
[22] J. Ma, Y. Song, H. Jiang, L. Rong, Effect of Cu on the microstructure and mechanical properties of a low-carbon martensitic stainless steel, Materials 15 (2022).
[23] F. Walther, Microstructure-oriented fatigue assessment of construction materials and joints using short-time load increase procedure, Mater. Test. 56 (2014) 519–527.
[24] F. Walther, D. Eifler, Cyclic deformation behavior of steels and light-metal alloys, Mater. Sci. Eng., A 468–470 (2007) 259–266.
[25] O. Gulbay, M. Ackermann, A. Gramlich, A.R. Durmaz, I. Steinbach, U. Krupp, Influence of transformation temperature on the high-cycle fatigue performance of carbide-bearing and carbide-free bainite, steel research int 94 (2023).
[26] M. Ferrari, L. Lutterotti, Method for the simultaneous determination of anisotropic residual stresses and texture by x-ray diffraction, J. Appl. Phys. 76 (1994) 7246–7255.
[27] D. Dengel, H. Harig, Estimation of the fatigue limit by progressively-increasing load tests, Fatig. Fract. Eng. Mater. Struct. 3 (1980) 113–128.
[28] A. Baqerzadeh Chehreh, M. Grätzel, J.P. Bergmann, F. Walther, Fatigue behavior of conventional and stationary shoulder friction stir welded EN AW-5754 aluminum alloy using load increase method, Metals 10 (2020) 1510.
[29] A. Giertler, U. Krupp, Investigation of fatigue damage of tempered martensitic steel during high cycle fatigue and very high cycle fatigue loading using in situ monitoring by scanning electron microscope and high-resolution thermography, steel research int 92 (2021) 2100268.
[30] H.K.D.H. Bhadeshia, D.V. Edmonds, Bainite in silicon steels: new composition–property approach part 1, Met. Sci. 17 (1983) 411–419.
[31] O. Gulbay, A. Gramlich, U. Krupp, Effects of silicon and aluminum alloying on phase transformation and microstructure evolution in Fe–0.2C–2.5Mn steel: insights from continuous–cooling–transformation and time–temperature–transformation diagrams, steel research int 95 (2024).
[32] L.C.D. Fielding, The bainite controversy, Mater. Sci. Technol. 29 (2013) 383–399.
[33] A. Grajcar, A. Kilarski, A. Kozlowska, Microstructure–property relationships in thermomechanically processed Medium-Mn steels with high Al content, Metals 8 (2018) 929.
[34] S.-H. Song, R. Faulkner, P. Flewitt, Quenching and tempering-induced molybdenum segregation to grain boundaries in a 2.25Cr–1Mo steel, Mater. Sci. Eng., A 281 (2000) 23–27.
[35] F.G. Caballero, C. Garcia-Mateo, M.J. Santofimia, M.K. Miller, C. García de Andrés, New experimental evidence on the incomplete transformation phenomenon in steel, Acta Mater. 57 (2009) 8–17.
[36] W.T. Reynolds, F.Z. Li, C.K. Shui, H.I. Aaronson, The incomplete transformation phenomenon in Fe-C-Mo alloys, MTA 21 (1990) 1433–1463.
[37] A. Gramlich, C. van der Linde, M. Ackermann, W. Bleck, Effect of molybdenum, aluminium and boron on the phase transformation in 4 wt.–% manganese steels, Results Mater. 8 (2020) 100147.
[38] J. Wang, P.J. van der Wolk, S. van der Zwaag, On the influence of alloying elements on the bainite reaction in low alloy steels during continuous cooling, J. Mater. Sci. 35 (2000) 4393–4404.
[39] S. Khare, K. Lee, H.K.D.H. Bhadeshia, Relative effects of Mo and B on ferrite and bainite kinetics in strong steels, Int. J. Mater. Res. 100 (2009) 1513–1520.
[40] E. Essadiqi, J.J. Jonas, Effect of deformation on the austenite-to-ferrite transformation in a plain carbon and two microalloyed steels, Metall. Trans. A 19 (1988) 417–426.
[41] J. Chen, S. Tang, Z. Liu, G. Wang, Influence of molybdenum content on transformation behavior of high performance bridge steel during continuous cooling, Mater. Des. 49 (2013) 465–470.
[42] J. Kong, C. Xie, Effect of molybdenum on continuous cooling bainite transformation of low-carbon microalloyed steel, Mater. Des. 27 (2006) 1169–1173.
[43] M. Peet, H. Bhadeshia, Program MAP_STEEL_MUCG83.
[44] Z. Chen, J. Qi, H. Liu, L. Sun, H. Wei, G. Wang, Bainitic transformation and mechanical properties of low-carbon high-strength bainitic steels with Mo addition, J. Mater. Eng. Perform. 29 (2020) 2428–2439.
[45] M. Ackermann, B. Resiak, P. Buessler, B. Michaut, W. Bleck, Effect of molybdenum and cooling regime on microstructural heterogeneity in bainitic steel wires, steel research int. 91 (2020).
[46] J. Wang, Z. Wang, X. Wang, Q. Yang, X. Jin, L. Wang, Strengthening effect of nanoscale precipitation and transformation induced plasticity in a hot rolled copper-containing ferrite-based lightweight steel, Scr. Mater. 129 (2017) 25–29.
[47] H. Song, J. Yoo, S.-H. Kim, S.S. Sohn, M. Koo, N.J. Kim, S. Lee, Novel ultra-high-strength Cu-containing medium-Mn duplex lightweight steels, Acta Mater. 135 (2017) 215–225.
[48] F. Meng, J. Wang, J. Guo, K. Fu, M. Zhao, Z. Wang, Z. Xu, Growth behavior and kinetics of austenite grain in low-carbon high-strength steel with copper, Mater. Res. Express 8 (2021) 96504.
[49] C. Antonione, G. Gatta, A. Lucci, G. Riontino, G. Venturello, The role of substitutional transition elements on recrystallization processes in dilute iron solid solutions, Acta Metall. 18 (1970) 1169–1180.
[50] J. Syarif, Z. Sajuri, Effect of copper addition on grain refinement of austenite in Fe-8wt.% Ni-(0-3) wt.% Cu alloy, Sains Malays. 39 (2010) 999–1006.

[51] N. Saeidi, M. Raeissi, Promising effect of copper on the mechanical properties of transformation-induced plasticity steels, Mater. Sci. Technol. 35 (2019) 1708–1716.
[52] J. Duan, Y. Ju, P. Dastur, C. Slater, M. Strangwood, C. Davis, Assessing the solute drag of scrap residual elements of Sn and Cu in austenite, J. Mater. Res. Technol. 40 (2026) 1275–1284.
[53] D.J. Dingley, D. McLean, Components of the flow stress of iron, Acta Metall. 15 (1967) 885–901.
[54] I. Gutiérrez, M.A. Altuna, Work-hardening of ferrite and microstructure-based modelling of its mechanical behaviour under tension, Acta Mater. 56 (2008) 4682–4690.
[55] O. Gulbay, A. Gramlich, U. Krupp, Impact toughness and fatigue crack propagation in carbide-free bainite: the adverse role of retained austenite and martensite-austenite islands, Fatig. Fract. Eng. Mater. Struct. 48 (2025) 4217–4227.
[56] B. Hu, H. Sui, Q. Wen, Z. Wang, A. Gramlich, H. Luo, Review on the plastic instability of medium-Mn steels for identifying the formation mechanisms of Lüders and Portevin–Le chatelier bands, Int. J. Miner. Metall. Mater. 31 (2024) 1285–1297.
[57] P. Mohseni, J.K. Solberg, M. Karlsen, O.M. Akselsen, E. Østby, Cleavage fracture initiation at M–A constituents in intercritically coarse-grained heat-affected zone of a HSLA steel, Metall. Mater. Trans. A 45 (2014) 384–394.
[58] F. Zhao, L. Morales-Rivas, Q. Yu, G. Wang, F.G. Caballero, D. San-Martin, Unforeseen influence of the prior austenite grain size on the mechanical properties of a carbide-free bainitic steel, Mater. Sci. Eng., A 881 (2023) 145388.
[59] H. Du, Y. Gong, T. Liang, Y. Li, Y. Xu, X. Lu, Q. Zeng, et al., Enhancement of impact toughness via tailoring deformation compatibility of constituent phases in duplex Q&P steel with excellent strength and ductility, Metall. Mater. Trans. A 51 (2020) 2097–2117.
[60] X. Zhou, W. Zhao, L. Dong, N. Song, Effect of quenching and tempering temperatures on microstructure and properties of ultrahigh strength cast steel, steel research int. 93 (2022).
[61] Y. Wang, G. Yuan, F. Xu, J. Kang, Z. Wu, W. Geng, D. Liu, et al., Effect of cooling medium on microstructure and properties of ultrahigh strength martensitic quenched and tempered steel, steel research int. (2025).
[62] N. Stanford, J. Wang, T. Hilditch, Quantification of strain partitioning during low cycle fatigue of multi-phase steels containing a bainite matrix, Int. J. Fatig. 129 (2019) 105218.
[63] G. Chai, N. Zhou, Study of crack initiation or damage in very high cycle fatigue using ultrasonic fatigue test and microstructure analysis, Ultrasonics 53 (2013) 1406–1411.
[64] Z. Cheng, A. Jiang, C. Cao, L. Cheng, W. Yu, In-situ investigation of crack initiation and propagation in bainite-martensite dual-phase microstructures, J. Mater. Res. Technol. 36 (2025) 2640–2651.
[65] G. Gao, R. Liu, K. Wang, X. Gui, R. Misra, B. Bai, Role of retained austenite with different morphologies on sub-surface fatigue crack initiation in advanced bainitic steels, Scr. Mater. 184 (2020) 12–18.
[66] K. Okada, K. Tsuzaki, E. Nakagawa, A. Shibata, Fatigue limit doubling in high-strength martensitic steel through crack embryo engineering-cyclic-training-driven self-optimization, Advanced science (Weinheim, Baden-Wurttemberg, Germany) 12 (2025) e04165.
[67] S. Ishihara, A. McEvily, A coaxing effect in the small fatigue crack growth regime, Scr. Mater. 40 (1999) 617–622.
[68] G.M. Martínez-Cázares, R.D. Mercado-Solís, R. Colás, N.F. Garza-Montes-de-Oca, High temperature oxidation of silicon and copper–silicon containing steels, Ironmak. Steelmak. 40 (2013) 221–230.